7

Vehicle Mounted Dual Sensor: SAR-GPR

Motoyuki Sato, Kazunori Takahashi, Takao Kobayashi,
Jun Fujiwara and Xuan Feng
Tohoku University
Japan

1. Introduction

Tohoku University, Japan has developed a new dual sensor SAR-GPR since 2002, which was designed to be used on a robotic arm mounted on an unmanned vehicle. SAR-GPR employs the combination of metal detector and GPR (Ground Penetrating Radar). Dual sensor is a common approach for landmine detection. However, imaging by GPR is very difficult in strongly inhomogeneous material due to strong clutter. We proposed therefore to use a Synthetic Aperture Radar (SAR) approach to solve this problem. SAR-GPR antennas are scanned mechanically near the ground surface and acquire the radar data. SAR-GPR uses an array antenna composed of 6 elements, in order to suppress the ground clutter. The data is then processed for subsurface imaging.

In order to achieve the optimum SAR-GPR performance, we believe that the adaptive selection of the operating frequencies is quite important, and that antenna mismatch causes serious problems in GPR. Most of the conventional GPR systems employ impulse radar, because it is compact and data acquisition is fast. However, most of the impulse radar system have disadvantages such as signal instability, especially time drift and jitter, strong impedance mismatch to a coaxial cable, which causes serious ringing, and fixed operating frequency range. An alternative way to solve this problem is the use of a vector network analyzer, which is a synchronized transmitter-receiver measurement equipment composed of a synthesizer and a coherent receiver. It enables quite flexible selection of operation frequencies, and stable data acquisition. We have therefore chosen to equip the SAR-GPR with 3 sets of vector network analyzer operating in the 100MHz-4GHz frequency range. The optimal operational range can actually be selected as a function of the soil conditions.

In this chapter, we discuss the concept of SARGPR, and its hardware development and software implementation. Then we show an example of field evaluation test which was held in Croatia in 2006.

2. Mine Hunter Vehicle (MHV)

SAR-GPR has been developed under a research project which was supported by JST (Japan Science and Technology Agency). In this project, Tohoku University has developed dual sensors including SAR-GPR, which is to be equipped on vehicles, and a hand-held dual sensor ALIS. Under the same research projects, unmanned vehicles which will be used for

Source: Humanitarian Demining: Innovative Solutions and the Challenges of Technology, Book edited by: Maki K. Habib, ISBN 978-3-902613-11-0, pp. 392, February 2008, I-Tech Education and Publishing, Vienna, Austria

demining sensors have been developed. Mine Hunter Vehicle (MHV) is one of them, which was developed by Chiba University and Fuji Heavy Industries. MHV was designed for safe access to minefields and scan sensors over the field.

(a) SAR-GPR mounted on a robotic arm and scans in front of the MHV.

(b) SAR-GPR in operation in CROMAC test site. SAR-GPR scans in the side of MHV

Fig. 1. Mine Hunter Vehicle (MHV) equipped with SAR-GPR

3. SAR-GPR Array Antenna System

3.1 Transmitting/Receiving Antenna

Anti-personnel (AP) mines are normally deployed in very shallow subsurface. In order to detect such AP mines, GPR is required to have a very wide frequency range to realize a fine range resolution so that the shallow target echo can be separated from the strong ground surface reflection. SAR-GPR covers the frequency range wider than 5GHz, which realizes the range resolution of the radar to be 2.5cm in air. Soil has larger dielectric constant than air, typically larger than $4\varepsilon_0$ which makes the range resolution in subsurface smaller than 1.25cm, where ε_0 is the dielectric constant of vacuum.

Vivaldi antenna shown in Fig. 2 (Langley, 1993) was adopted as transmitting and receiving antennas for SAR-GPR, primarily due to its wide frequency performance. Fig.3 shows the return loss of the optimized Vivaldi antenna, which is used for SAR-GPR. We can find that the return loss above 1GHz is over 10dB, and it works efficiently over a very wide frequency. And a very narrow transmitting pulse can be realized in the time domain as shown in Fig.4.

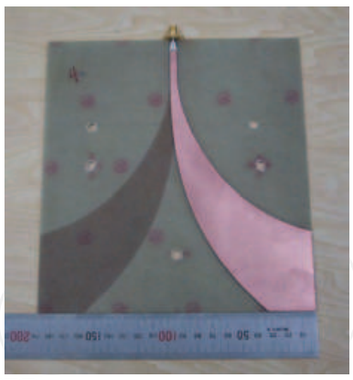

Fig.2 Vivaldi antenna for SAR-GPR

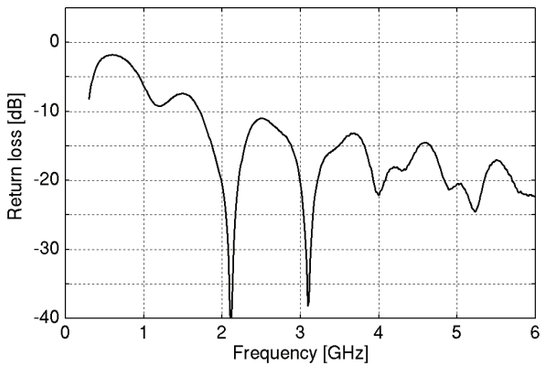

Fig.3. Return loss of the Vivaldi antenna shown in Fig.2.

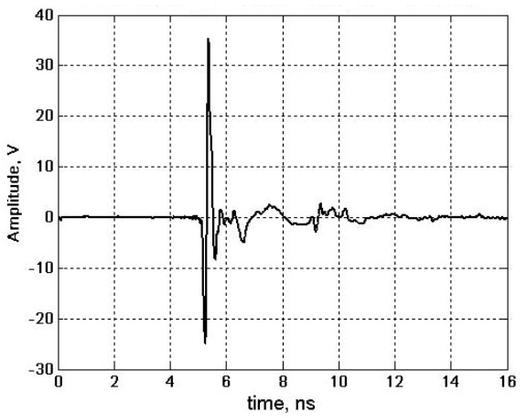

Fig. 4. Time domain waveform of the SAR-GPR radar pulse

3.2 CMP Array

The array antenna of SAR-GPR consists of three pairs of transmitting/receiving antennas as shown in Fig. 5. They are arranged in the Common Mid Point (CMP) arrangement where each antenna pair is placed on the base line symmetrically regarding to the common mid point. The CMP arrangement enables one easily apply CMP stacking technique (Yilmaz, 1987) to data processing which reduces strong surface clutter while enhancing subsurface object echo.

A Vivaldi antenna has planar shape thus is easily manufactured to construct an antenna array shown in Fig. 5. On the other hand, however, when it operates in an array structure, the antenna performance considerably suffers the antenna mutual coupling to adjacent antennas of which effect depends on the antenna spacing. In addition, CMP stacking performance also depends on the antenna spacing. Therefore, antenna spacing should be carefully determined to optimize the array system.

In order to determine the optimal antenna spacing, we evaluate the effect of antenna spacing on CMP stacking performance under rough surface and the effect of antenna spacing on the antenna efficiency of the Vivaldi antenna by model simulations.

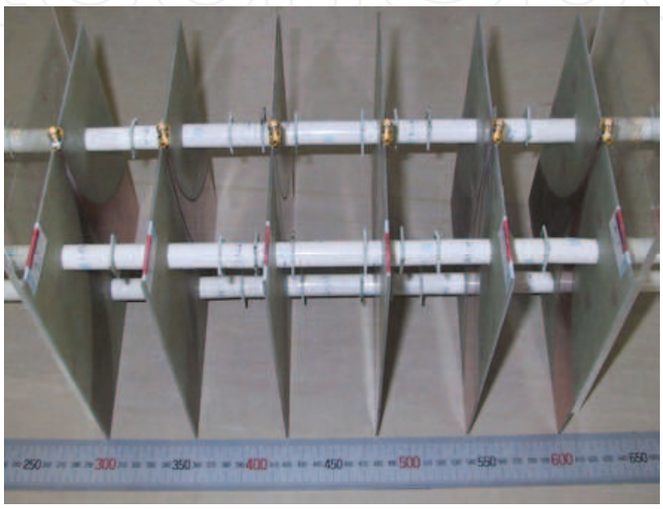

Fig. 5. SAR-GPR antenna array. The array system is installed in an antenna casing

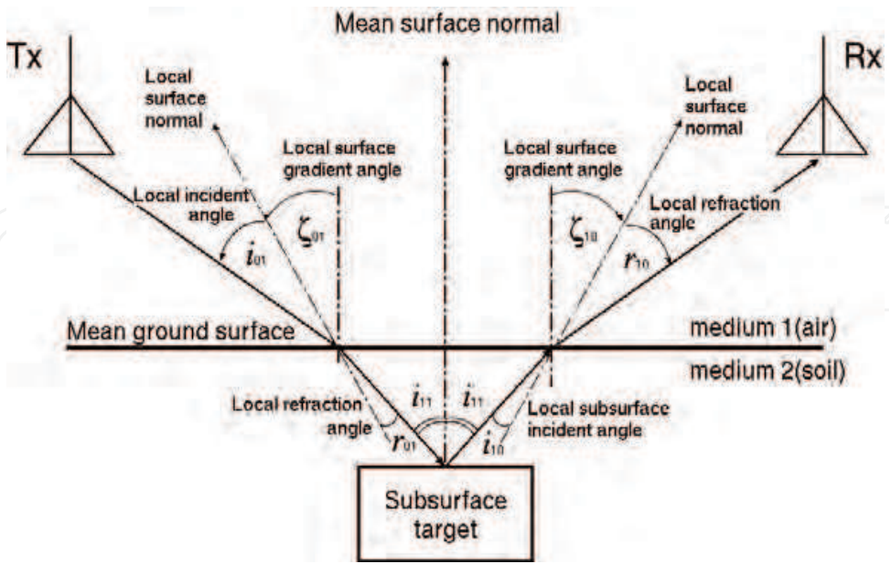

Fig. 6. Schematic diagram of the geometrical optics model

3.3 Geometrical Optics Model

The effect of antenna spacing on CMP stacking performance under rough surface condition was evaluated by a geometrical optics model. Fig.6 shows a schematic sketch of the model. Air and soil; two media model was considered. A one dimensionally rough surface, namely, corrugated surface, was assumed to be the media boundary interface.

The transmission antenna was modeled as a point source antenna that transmits a spherical wave pulse of an unit amplitude. The propagation path of the pulse was defined by Snell's law. Fresnel's coefficients of reflection/refraction at the incident point on the boundary interface and on the subsurface target determine subsurface echo amplitude. The effect of the ground surface roughness was taken into account by the local surface gradient at the incident point of the radar pulse. Height distribution of the rough surface was not considered. Subsurface target was assumed to have a flat horizontal surface and to be located on the CMP lines of the CMP array antenna. Therefore, provided the incident angle of the radar pulse onto the ground surface, refraction angle at the air-ground boundary interface, reflection angle on the target surface, incident angle at the ground-air boundary interface are uniquely determined in order that the subsurface echo should be received by the receiving antenna.

3.4 Target Echo

We consider the problem in the plane that contains both transmitting and receiving antennas and the target. The amplitude of the subsurface target echo A under given incident angle θ was calculated by the following:

$$A(\theta) = T_{01}(\theta) \cdot R_{\text{Target}}(\theta_{11}) \cdot T_{10}(\bar{\theta}) \cdot \frac{1}{R} \tag{1}$$

where T_{01}, R_{Target}, and T_{10} are Fresnel's coefficient of refraction at the air-ground interface, reflection at the subsurface target face, and refraction at the ground-air interface, respectively. Horizontally polarized electric field was assumed. θ_{11}, $\bar{\theta}$ are the incident angle on the subsurface target and the local incident angle of the subsurface echo pulse onto the ground surface from subsurface, respectively. R is the geometrical distance measured along the propagation path. Since the target was assumed to be located on the CMP line and that both transmission antenna and the receiving antenna were located symmetrical position to the CMP line, the propagation path was uniquely determined once the incident angle θ was given. Furthermore, the incident angle θ is the only independent variable due to the symmetry of the problem, therefore, all the terms in the right hand side in (1) are dependent variables on θ. Considering the statistical property of Gaussian random rough surface, we evaluate the statistical expectation of the subsurface target echo by integrating $A(\theta)$ with the weighting of the Gaussian distribution function of local surface gradient, $P(\theta)$, as

$$\langle A \rangle = \int_0^{\pi/2} P(\theta) T_{01}(\theta) \cdot R_{\text{Target}} \cdot P(\theta_{11}) T_{10}(\bar{\theta}) \cdot \frac{1}{R} d\theta \quad . \tag{2}$$

The distribution function of surface gradient of a Gaussian random rough surface also has the form of a Gaussian (Ogilvy, 1991). $P(\theta)$ is written as

$$P(\theta) = \frac{1}{\sqrt{2\pi}\tan\theta_{RMS}} \exp\left\{-\frac{1}{2}\left(\frac{\tan\theta}{\tan\theta_{RMS}}\right)^2\right\} \tag{3}$$

where θ_{RMS} is the RMS gradient of the surface of concern. The integration was carried out from 0 to $\pi/2$ in accordance with the possible incident angle. Note that $P(\theta)$ appears twice in (2) corresponding to that, due to the symmetry of the problem, the local surface gradient at the two incident points on the ground surface must have the same absolute value but with opposite signs.

3.5 Antenna Efficiency

Closely arranged antennas have strong mutual coupling that gives effect on radar pulse transmission of the antenna. We defined the antenna efficiency by the maximum amplitude of the transmitted radar pulse. And we numerically investigated it by FDTD simulations shown in Fig. 7 finally to model the antenna efficiency, W, as a function of the antenna spacing, d, as follows:

$$W(d) = \begin{cases} 0.2 + \frac{1}{2}\left[1 - \cos((d-2)/8 \cdot \pi)\right] & (2\,\text{cm} \le d \le 10\text{cm}) \\ 1.2 \quad (d > 10\text{cm}) \end{cases} \tag{4}$$

3.6 CMP Amplitude

Finally, the CMP signal amplitude of the target, A_{CMP}, for the case of the antenna spacing of d cm was calculated from (2) and (4) as

$$A_{CMP}(d) = W(d)\sum_n \langle A \rangle_n \tag{5}$$

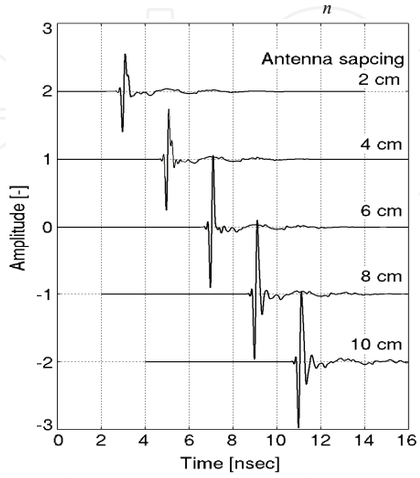

Fig. 7. Time domain waveforms of transmitted pulse for various antenna spacing cases

where n refers to the number of the nth antenna pair of the CMP array. In calculation of $\langle A \rangle$, we assumed a Gaussian random rough surface with 54degrees RMS gradient, in other words it had the same value of RMS height and correlation distance.

3.7 Confirmation by Full Scale Simulations

FDTD simulation of CMP measurement was carried out with a full scale model. The Vivaldi antenna array was modeled in the real scale. The position of the antenna in the present paper was defined as the antenna stand off that was set 10cm as had been designed to do in actual field measurements.

The air-ground interface was a Gaussian random rough surface whose RMS gradient was 54 degrees. Two dimensional height distribution was considered for several roughness scale cases. The roughness scale, or the RMS height was changed from 5mm to 4cm but keeping the RMS gradient as 54 degrees. Five independent surface realizations were numerically generated for each roughness scale case and examined.

Antenna spacing was investigated from 2cm to 10cm with 2cm interval. The subsurface target had the pancake shape whose diameter was 8cm and whose thickness was 4cm, which were the same as those of Type-72 AP mine. The target was embedded in subsurface horizontally so that its upper face was at the depth of 6cm. The dielectric constant of the target was set $3\varepsilon_0$ and that of subsurface medium was $4\varepsilon_0$. Fig. 8.. shows the CMP amplitude of the subsurface target. Those results from different scale surface realizations were plotted together. The result of the geometrical optics model is also plotted for comparison.

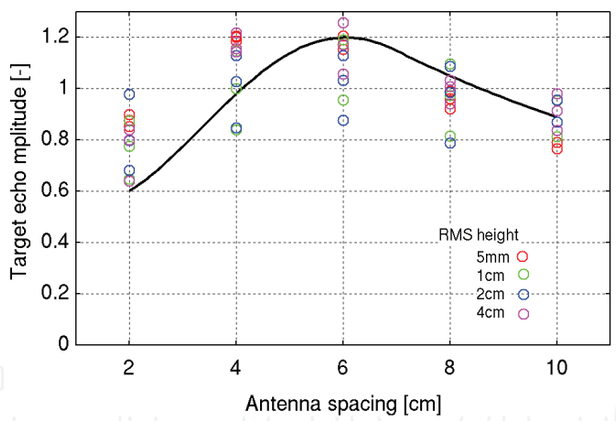

Fig. 8. Comparison of the estimated CMP target echo amplitude (solid line) and full scale FDTD simulation results (colored open circles). The color of circles denotes the roughness scale (RMS height) of the ground surface. Note that both are in a good agreement

Considering the fluctuation of random phenomena, the FDTD simulation results and numerical estimation show a good agreement: CMP signal amplitude behaves as a function of antenna spacing and has a maximum at 6cm of the antenna spacing. Receiving this result, the antenna spacing of the CMP antenna array system of the SAR-GPR was finally determined as 6cm.

4. Image Reconstruction

Two stage signal processing was carried out after the acquired data was transformed into time-domain data by inverse Fourier transformation. At first, the CMP stacking was carried out for suppression of ground clutter. In this processing, 5 data sets acquired at one position is stacked by calculating the time delay differences due to different propagation length between antenna sets. Clutter from the ground surface and homogeneous gravel can be suppressed by this CMP processing. The stacked signal is then processed by the diffraction stacking algorithm and a 3D image is reconstructed. The diffraction stacking is one of the standard migration algorithms used for GPR and seismic measurement. The reconstructed image $P(x, y, z)$ by the diffraction stacking is given by

$$P(x, y, z) = \int f(\tau, x', y')dx'dy' \tag{6}$$

where $f(\tau, x', y')$ is the measured signal at the antenna position $P_A(x', y')$ at time $t = \tau$ where

$$\tau = \frac{2\sqrt{(x-x')^2 + (y-y')^2 + z'^2}}{v} \tag{7}$$

is the travel time from the antenna position $P_A(x', y')$ to the focusing point $P(x, y, z)$, and v is the assumed velocity of wave in the material.

At the same time, we developed more advanced signal processing which can be used together with SAR-GPR(Sato, et.al., 2004). We can also use the GPR data set for estimation of ground surface topography, and estimation of velocity model, which can be implemented in the image reconstruction algorithm. If the ground surface is not flat, we can adopt more sophisticated signal processing for 3-D image reconstructions (Feng & Sato 2004, Feng et. al, 2005).

5. Compact VNA

In order to achieve the optimum SAR-GPR performance, selection of adaptive operational frequency is quite important. Also, antenna mismatching causes serious problems in GPR. Most of the conventional GPR systems employed impulse radar, because it is compact and data acquisition is fast. However, most of the impulse radar system had disadvantages such as instability in signal, especially time drift and jitter, strong impedance mismatching to a coaxial cable, which causes serious ringing, and fixed frequency range. Vector network analyzer is a synchronized transmitter- receiver measurement equipment. It is composed of a synthesizer and coherent receiver. It enables quite flexible selection of operation frequencies, and stable data acquisition. In addition, commercial vector network analyzers are equipped with a calibration function, which masks impedance mismatching caused by RF hardware. Impedance matching of antennas to coaxial cables in GPR is quite difficult in all the frequency range of operation. Therefore refection caused by impedance mismatching

returns to a generator, and signal wave deforms. In order to avoid these effects, many GPR antennas adopt strong damping by impedance loading, which decreases antenna efficiency. If we use a vector network analyzer, reflection from antennas can be perfectly absorbed by the vector network analyzer, therefore, we can operate antennas without heavily impedance loading.

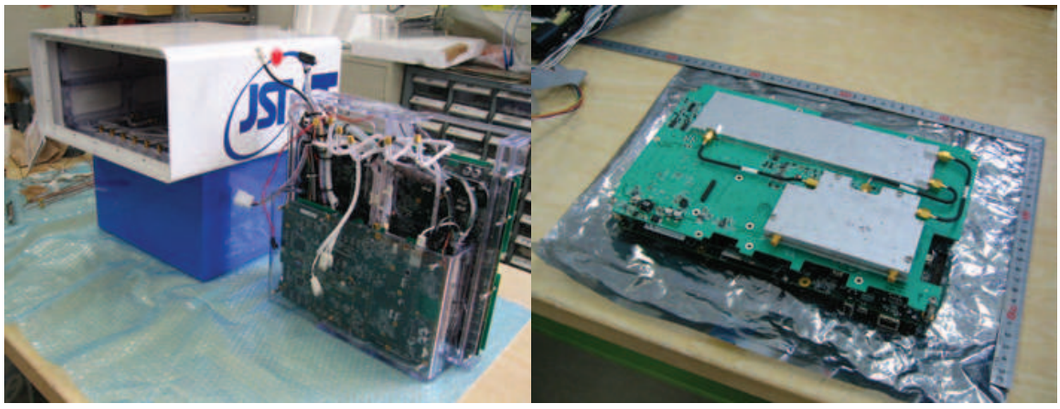

(a) Three vector network analyzers mounted in SAR-GPR

(b) One unit of a compact vector network analyzer

Fig. 9. Compact Vector Network Analyzer. (VNA)

However, due to the large size and weight, conventional network analyzer cannot be mounted in SAR-GPR. Compact vector network analyzer has been available, which can be used field measurement, however, these existing compact vector network analyzer had a limited frequency range, which cannot be adopted in GPR for landmine detection, and data acquisition speed was too slow for practical use. Therefore, we developed a new compact vector network analyzer which fits to our requirements. Table 1. show the comparison of the specifications of commercial and new vector network analyzers.

	Developed VNA	MS4624	E5071B
Measurement	S21	S21,S11,S22	S21,S11,S22
Operation condition	-20 - +50C		
Frequency	100MHz-4GHz	10MHz-9GHz	300kHz-8.5GHz
Dynamic range	70dB	125dB	122dB
Acquisition rate	646pt/sec	6,500pts/s	1,000,000pts/s
Accuracy	±1dB	±1.5dB	±1dB
Power supply	DC12-15V10W	100-200V,540W	100-200V
Size	250x170x60	352x222x457	
Weight	1.7kg	25kg	17.5kg

Table 1. Comparison of commercial and developed vector network analyzers (VNA)

The SAR-GPR system is composed of the array antenna and 3 sets of vector network analyzer. The system configuration can be found in Fig.9(a). Three vector network analyzer boards shown in Fig.9(b) is placed in a box , and are connected to the antennas just below the vector network analyzers. The total size of the system is 40Cm x 40cm x 40cm and the weight is 15kg.

6. Experimental Results

6.1 Laboratory Experiments

Laboratory experiments were carried out at a sandpit in the GPR Lab., Center for Northeast Asian Studies, Tohoku University, Japan. This sandpit is 4m x 4m x 1m (depth) . The targets were landmine models Type 72 and PMN-2 shown in Fig. 10 and a *mine-like*[1] stone, which were buried in the layout shown in Fig. 11. They were all buried at a depth of 2 cm[2], and the landmine model PMN-2 was vertically buried. The soil was dry sand mixed with gravels whose diameters were approximately 2 cm. The GPR antennas were scanned at a velocity of 100 mm/s. The interval of data acquisition was 30 mm in both x- and y-directions.

(a) Type 72 (b) PMN-2

Fig. 10. Landmine models used in laboratory evaluation

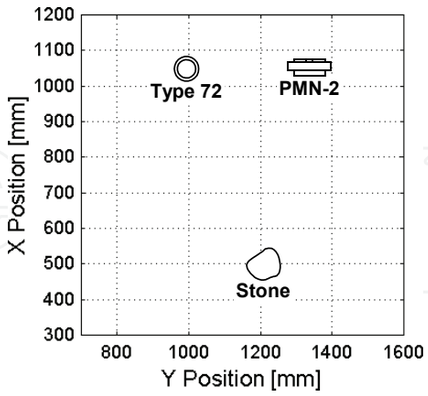

Fig. 11. Layout of the buried landmine models. PMN-2 landmine model was vertically buried

[1] The term *mine-like* object is defined as an object whose shape and dimension resemble that of a landmine.

[2] A buried depth is defined at the top of a target.

The raw GPR data acquired with the inner pair of the antennas is transformed into time domain and is shown in Fig. 12 as a horizontal slice (C-scan) at a time instance of 2.4 ns, which corresponds to a depth of about 2 cm. The three objects are hardly visible, and clutter can be seen. The responses from the targets are not clear and not round shaped. They thus cannot be recognized without *a priori* knowledge. Then the subsurface image was reconstructed by migration. Fig. 13 shows a horizontal slice (C-scan) of the processed data at a depth of 2 cm. The three targets are clearly imaged and they obviously have different shapes and dimensions than those of clutter imaged at left on the slice.
The measurement was a blind test, i.e. the operator did not know the types, positions, depths, and numbers of buried objects prior to the measurement and only the radar system was tested. By observing the data, the operator could detect all of the objects including the stone on site.

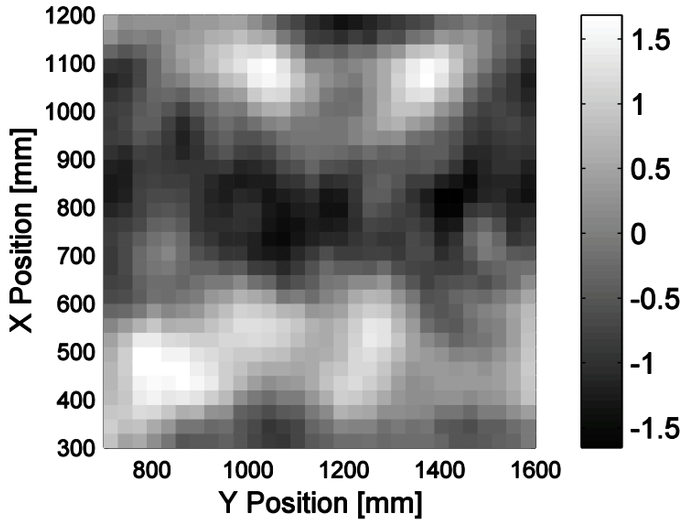

Fig. 12. Horizontal slice (C-scan) at a time instance of 2.4 ns measured with the inner pair of the antennas. The time of 2.4 ns corresponds to a depth of 2 cm

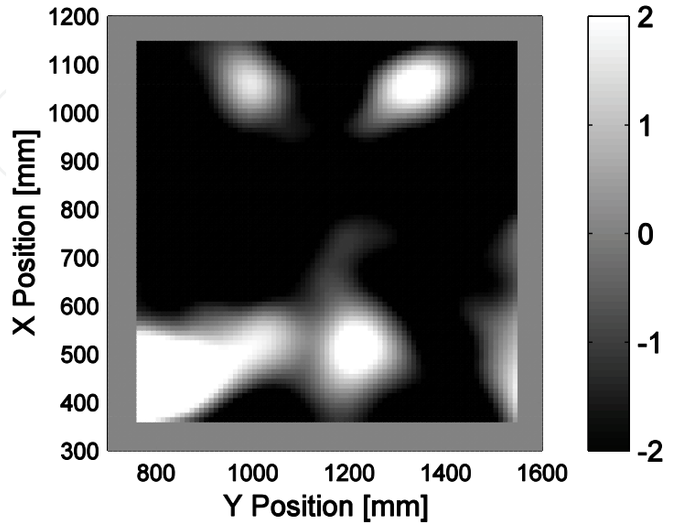

Fig. 13. Reconstructed horizontal slice image (C-scan) by migration. 2 cm depth

6.2 Field Trial

An evaluation trial was conducted in Croatia during February – March 2006 (Ishikawa et al., 2006). The campaign was organized by Japanese Science and Technology Agency (JST), which is a subordinate organization of Japanese Ministry of Education, Science and Technology, and was in cooperation with Croatian Mine Action Centre, Centre for Testing, Development and Training (CROMAC-CTDT).

The trial was carried out at a test site of CROMAC-CTDT in Benkovac, Croatia. Three lanes (Lane #1, #3, and #7) were chosen to evaluate the performances in various soils. The lanes have mineralized and homogeneous soil, natural and homogeneous soil, and mineralized and heterogeneous soil containing stones, respectively (see Guelle et al., 2007 and Preetz & Igel, 2006 for more detailed descriptions of the soils). During the trial, the relative permittivity of the soil was more than 20, sometimes more than 40 after raining and snowing. All the lanes are 1 m wide and 50 m long.

Two kinds of former Yugoslavian anti-personnel landmines, PMA-1A and PMA-2 shown in Fig. 14 and Table 2, were exploited as targets. The landmines were inert and real with the first explosives in the detonators removed and the inner structures intact. In addition, a standardized metal clutter, ITOP I0 (CEN, 2003), and small piece of random-shaped metals were also buried as representatives of metal clutters.

Fig. 14. PMA-1A (left) and PMA-2 (right) used in the trial

	PMA-1A	PMA-2
Weight	400 g	135 g
Explosive weight, type	200 g, TNT	100 g, TNT
Fuze	UPMAH-1	UPMAH-2
Size	140 (L), 30 (H), 70 (W) mm	68 (D), 61 (H) mm
Operation pressure	3 kg (min)	7 – 15 kg
Detectability	Very difficult	Very difficult

Table 2. Specifications of the landmines used in the trial (King, 2003)

In order to construct a dual sensor system, a commercial metal detector (MIL-D1) was mounted on the robotic arm together with SAR-GPR radar. Due to the limitation of the arm movement, an area of approximately 1.1 x 1.2 m was surveyed at a vehicle position, and then the vehicle moved to scan the neighboring area. The area of the next scan is overlapped approximately 1.1 x 0.2 m. The surveyed areas of the metal detector and the radar have a 0.5 m shift.

Examples of the surveys are shown in Figs. 15– 20. The data shown is taken from in Lane #3, which is natural and homogeneous soil.

Fig. 15 shows the metal detector image and its interpretation. In principle, a metal response can be observed in an image as positive and negative valued two semi-circles because of the coil configuration. Four responses can be recognized at locations marked A – D in this example. Note that a discontinuity at y = 700 mm is caused by combining two images scanned separately on two neighboring areas. Fig. 16 shows a horizontal slice (C-scan) of processed GPR data at a depth of 75 mm in the same area of Fig. 15 and its interpretation. Two round-shaped contrasts can be found in this image (marked B and C). They can also be seen in the metal detector image (Fig. 15), and we therefore are able to recognize that they are landmines. Since a high contrast marked E is not round shaped but is continued from left to right, it is a topographic change. Landmines in areas marked A and D are buried at different depths, resulting that no contrasts for them are observed at this depth but they are visible in other slices at different depths.

Data acquired at another area in the same lane is shown in Figs. 17 and 18. In the metal detector image (Fig. 17), three responses can be seen. In this step, however, it cannot be identified whether it is a landmine or metal clutter. The GPR image (Fig. 18) has only two contrasts at the areas marked F and G and no contrast can be seen at the area E even a clear metal response appears in the metal detector image. This metal response is, thus, identified as metal clutter.

The ground truths for these areas are shown in Fig. 19. Note that the ground truth was provided after the surveys and the interpretations, and the trial was therefore completely blind tests. The data were interpreted by observing the series of horizontal slices (C-scan) at all the depths and the vertical slices (B- and D-scan) as well. It is impossible to make a decision by observing only one slice. Moreover, images are colored in the real interpretations.

Fig. 20 shows examples of fused image of the metal detector and the radar images. By displaying metal detector intensity as contour lines overlaid on a radar image, the locations of the responses in the two sensors are easily compared.

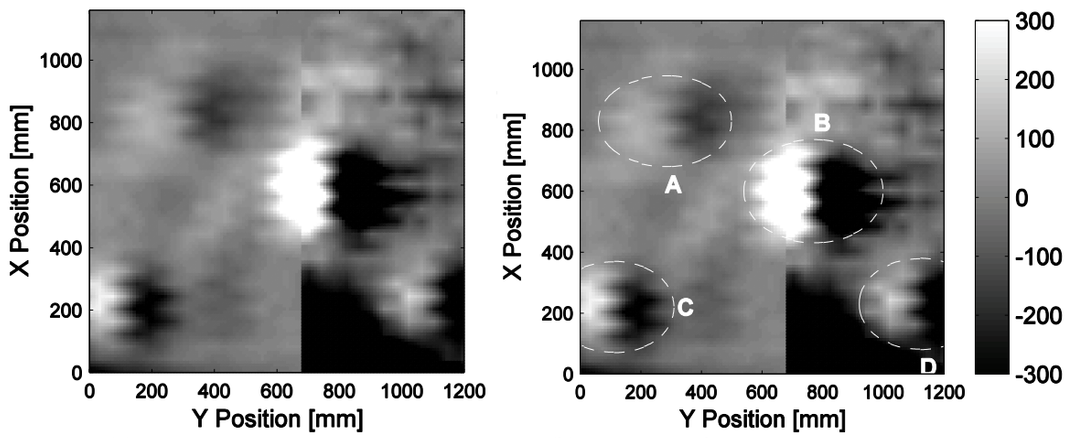

(a) Raw Image. (b) Interpretation.

Fig. 15. Metal detector image. The discontinuity at y = 700 mm is caused by combining two images separately scanned on two neighboring areas

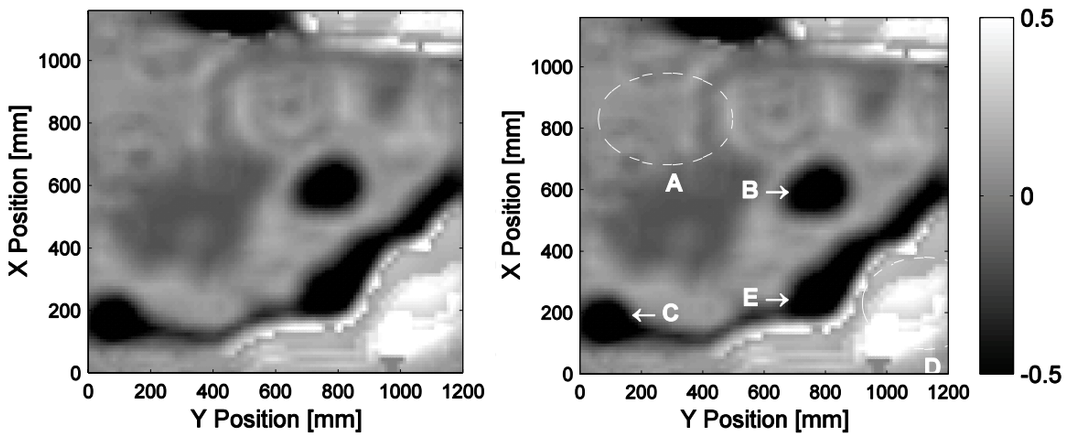

(a) Processed Image. (b) Interpretation.

Fig. 16. GPR Image at a depth of 75 mm

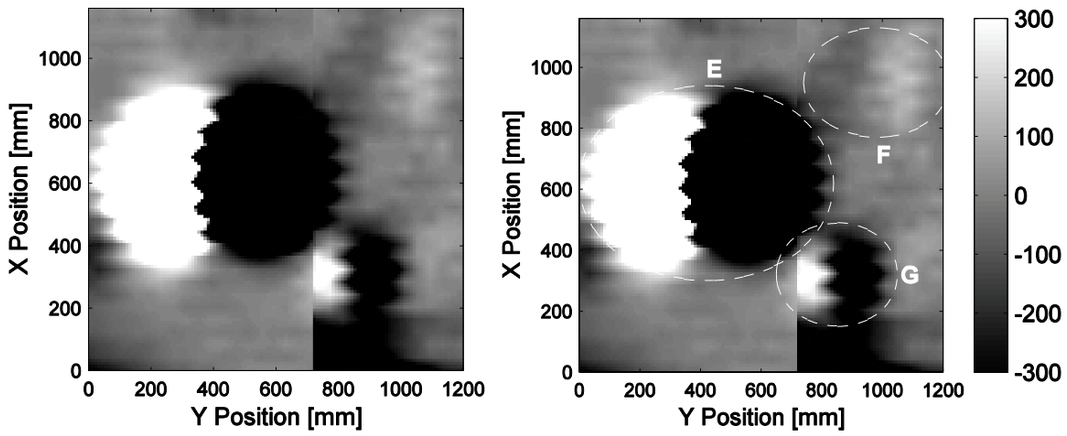

(a) Raw Image (b) Interpretation

Fig. 17. Metal detector image. The discontinuity at y = 700 mm is caused by combining two images separately scanned on two neighboring areas

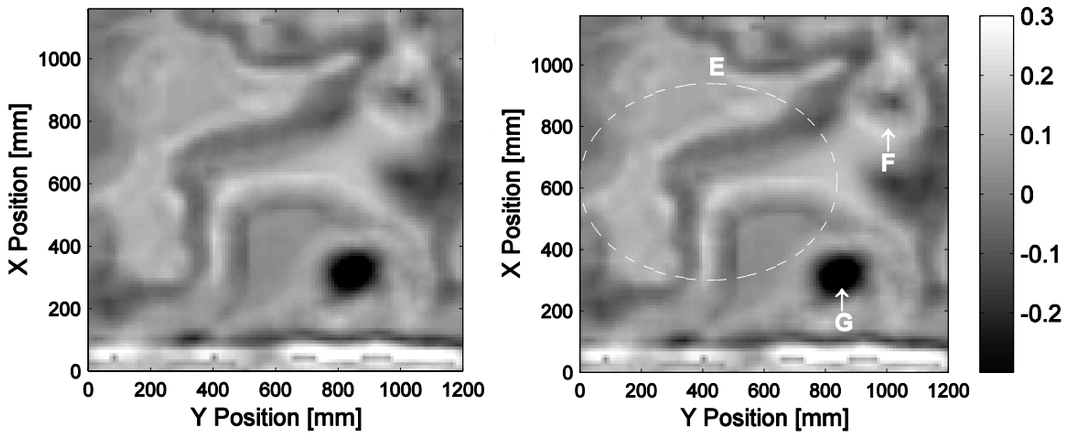

(a) Processed Image (b) Interpretation

Fig. 18. GPR Image at a depth of 87 mm

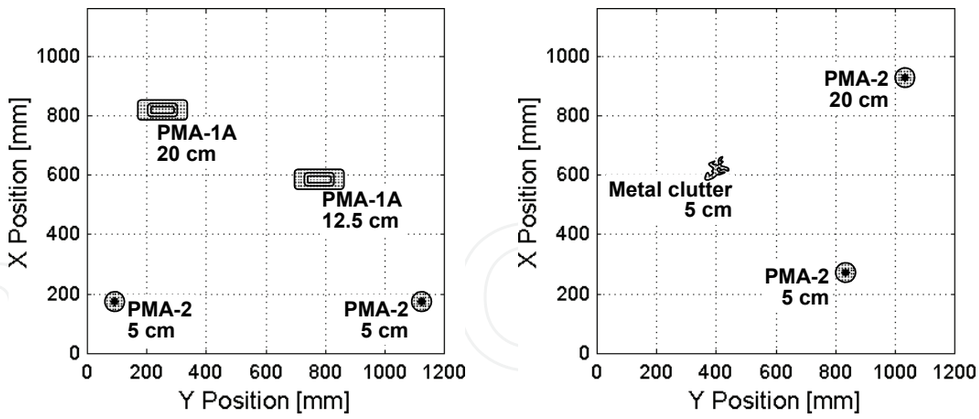

(a) The area shown in Figs 15 and 16. (b) The area shown in Figs. 17 and 18.

Fig. 19. The Ground truth

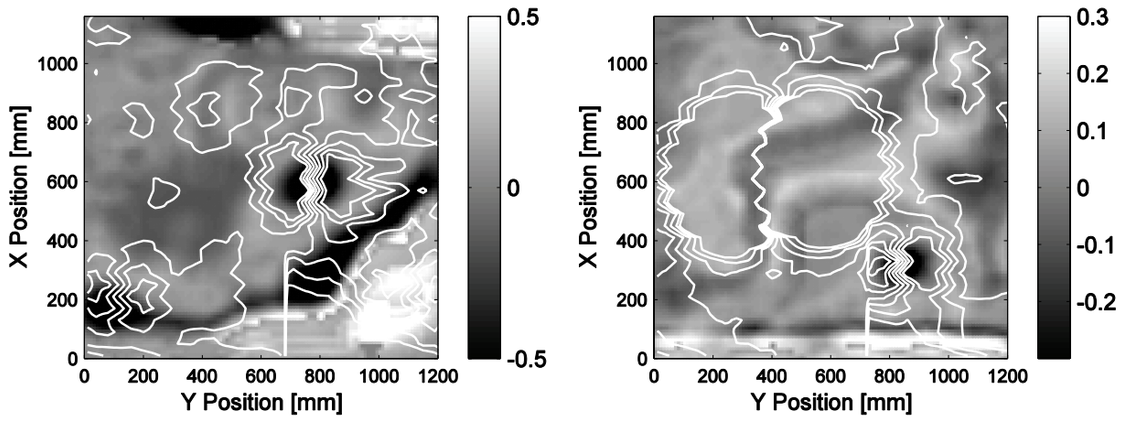

(a) The area shown in Figs 15 and 16. (b) The area shown in Figs. 17 and 18.

Fig. 20. An example of the image fusion of the metal detector and GPR images. Contour lines show metal detector intensity and are overlaid on the horizontal GPR image

7. Conclusion

SAR-GPR, which is an array GPR sensor unit, which is to be used on an unmanned vehicle MHV was developed by Tohoku University. It is equipped with 3 VNAs, and has 3 pairs of Vivaldi antenna. The operation frequency of the system can be selected between 100MHz-4GHz, dependent on the soil characteristics. Signal processing including CMP and migration is applied to the acquired GPR signal, and they reduce the clutter and can image the buried targets.

Then SAR-GPR has been tested in test sites in Japan, the Netherlands and Croatia. In any cases, SAR-GPR could provide clear images of buried landmines, when the ground has relatively flat surface. Since the SAR-GPR has 10cm offset above the ground surface, it can separate the reflection image of the ground surface and subsurface objects. Now we are continuing development new algorithms which can be used such a rough ground surface conditions.

8. Acknowledgements

This work was supported by JST (Japan Science and Technology Agency). A part of this work is also supported by JSPS Grant-in-Aid for Scientific Research (S)14102024 and (S) 18106008.

9. References

CEN (2003). *CEN (Comité Européen de Normalisation) Workshop Agreement, Humanitarian Mine Action - Test and Evaluation - Metal Detectors, CWA 14747*, available at http://www.itep.ws/pdf/CWA_metal_detectors.pdf

Guelle, D., Gaal, M., Bertovic, M., Müller, C., Scharmach, M. & Pavlovic, M. (2007). South-east Europe interim report field trial Croatia (STEMD-continuation), *ITEP Report*, available at http://www.itep.ws/pdf/STEMD_Interim_Croatia_final.pdf

Feng, X. & Sato, M.(2004), Pre-stack migration applied to GPR for landmine detection, *Inverse problems*, 20, 1-17.

Feng,X, Zhou,Z, Kobayashi, T., Savelyev, T., Fujiwara, J. & Sato, M.(2005), Estimation of ground surface topography and velocity models by SAR-GPR and its application to landmine detection, *Proc. Detection and remediation technologies for mines and minelike targets X*, March 2005, Orlando, FL, USA.

Ishikawa, J., Kiyota, M., Pavkovic, N. & Furuta, K. (2006). Test and evaluation of Japanese GPR-EMI dual sensor systems at Benkovac test site in Croatia, *JST Technical Report*, available at http://www.itep.ws/pdf/JapaneseTrialsCroatia2006.pdf

King, C. (2003). *Jane's mines and mine clearance 2003-2004*, Jane's Information Group, ISBN 0 7106 2555 3, Surrey UK

Langley, J. D.; Hall, P. S. & Newham, P. (1993) "Novel ultrawide-bandwidth Vivaldi antenna and low crosspolarization", *Electronics Letters*, 29, 2004-2005

Ogilvy, J. A.(1991) Theory of Wave Scattering from Random Rough Surfaces, Institute of Physcis Publishing, ISBN 0-7503-0063-9, Bristol

Sato, M., Hamada, Y., Feng, X., Kong, F., Zeng, Z., & Fang, G., (2004), GPR using an array antenna for landmine detection, *Near Surface Geophysics*, 2, 3-9.

Preetz, H. & Igel, J. (2006). Pedological description and magnetic susceptibility of the natural soil nearby the test site of the Croatian mine action centre (CROMAC) in Benkovac, Croatia, *Technical Report*, available at http://www.gga-hannover.de/app/gga_appl/produkte_docs/20070116105453.pdf

Yee, K. S.(1966) Numerical solution of initial boundary value problems involving Maxwell's equations, *IEEE Transaction of Antennas and Propagation*, 14, 302-307

Yilmaz, Ö.(1987) *Seismic Data Analysis*, Society of Exploration Geophysicists, ISBN 1-56080-094-1, Tulsa, U.S.A.

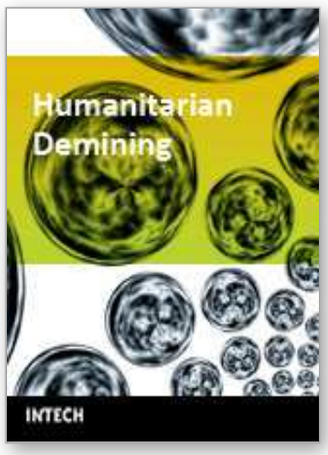

Humanitarian Demining

Edited by Maki K. Habib

ISBN 978-3-902613-11-0
Hard cover, 392 pages
Publisher I-Tech Education and Publishing
Published online 01, February, 2008
Published in print edition February, 2008

United Nation Department of Human Affairs (UNDHA) assesses that there are more than 100 million mines that are scattered across the world and pose significant hazards in more than 68 countries. The international Committee of the Red Cross (ICRC) estimates that the casualty rate from landmines currently exceeds 26,000 persons every year. It is estimated that more than 800 persons are killed and 1,200 maimed each month by landmines around the world. Humanitarian demining demands that all the landmines (especially AP mines) and ERW affecting the places where ordinary people live must be cleared, and their safety in areas that have been cleared must be guaranteed. Innovative solutions and technologies are required and hence this book is coming out to address and deal with the problems, difficulties, priorities, development of sensing and demining technologies and the technological and research challenges. This book reports on the state of the art research and development findings and results. The content of the book has been structured into three technical research sections with total of 16 chapters written by well recognized researchers in the field worldwide. The main topics of these three technical research sections are: Humanitarian Demining: the Technology and the Research Challenges (Chapters 1 and 2), Sensors and Detection Techniques for Humanitarian Demining (Chapters 3 to 8), and Robotics and Flexible Mechanisms for Humanitarian Demining respectively (Chapters 9 to 16).

InTech Europe
University Campus STeP Ri
Slavka Krautzeka 83/A
51000 Rijeka, Croatia
Phone: +385 (51) 770 447
Fax: +385 (51) 686 166

InTech China
Unit 405, Office Block, Hotel Equatorial Shanghai
No.65, Yan An Road (West), Shanghai, 200040, China
中国上海市延安西路65号上海国际贵都大饭店办公楼405单元
Phone: +86-21-62489820
Fax: +86-21-62489821

IntechOpen

IntechOpen